Methodology for Multipath-Component Tracking in Millimeter-Wave Channel Modeling

Chiehping Lai, Ruoyu Sun, *Senior Member, IEEE*, Camillo Gentile, *Member, IEEE*, Peter B. Papazian, *Senior Member, IEEE*, Jian Wang, and Jelena Senic

***Abstract*— We describe an extensive channel-measurement campaign, including 325 unique transmitter–receiver configurations, conducted in a lecture room with our 3-D double-directional 60 GHz channel sounder. The receiver was mounted on a mobile robot, with 40 cm spacing between channel acquisitions, enabling the tracking of clustered multipath components in the multidimensional delay-angle space. To mitigate against angle-estimation error and multipath blockage, we introduce a robust tracking algorithm based on the Assignment Problem. For the purpose of validation, the clusters were transformed from the delay-angle space onto a 2-D map of the environment and compared against the locations of cluster-generating reflectors, such as walls and tables. The location errors were typically within 30–50 cm. The clusters identified were then reduced to a stochastic map-based channel model, including reflection loss and dispersion characteristics such as the Ricean K-factor and angular spread. Given the 0.5 ns delay resolution of the channel sounder and angle-estimation error around 2°, the parameters were reported with high fidelity.**

***Index Terms*— Assignment Problem, Hungarian algorithm, millimeter-wave (mmWave), wireless.**

I. Introduction

THE seminal work by Saleh and Valenzuela [1] describes a stochastic model for the dispersion characteristics of indoor radio frequency channels through the clustering of multipath components (MPCs) in delay. To deliver spatial consistency necessary for the design of multiple-input multiple-output (MIMO) systems, the models have since evolved into geometry-based models for sub-6 GHz bands [2]–[4] and subsequently for millimeter-wave (mmWave) bands [5]–[9]. These models are still cluster based, but extend the property space of MPCs from delay only to double-directional angle, i.e., angle-of-departure (AoD) and angle-of-arrival (AoA) at the respective transmitter (TX) and receiver (RX). Cluster centroids correspond to locations of reflectors in the delay-angle space and the distribution of multipath within clusters describes the dispersion characteristics of the reflectors.

A preliminary step in the reduction of channel models from measured data is clustering the MPCs. Traditionally this has been carried out through human visual inspection, but now that channel sounders can collect hundreds or thousands of channel acquisitions due to advanced technology, automated processing is essential. Moreover, when sounders are mounted on a mobile platform, clusters originating from the same reflector must be identified across channel acquisitions—or tracked—in order to ensure temporal consistency.

Tracking radio frequency MPCs has its origins in radar, localization, and object identification [10], in particular, using ultrawideband (UWB) technology. UWB offers excellent delay resolution to discriminate propagation paths between closely spaced scatterers, yet low enough center frequency to penetrate walls and other obstructions [11]–[13]. Many tracking algorithms pose the problem within a probabilistic framework, often using particle filters [14]–[21]. Under the assumption of random Gaussian noise for measurement error, the problem can be solved through extended Kalman filtering [22]. The results in the above-cited papers are based on simulations alone, not actual measurements.

The cited papers in the sequel, rather, all have results from real measurements in the sub-6 GHz range. In the first three [23]–[25], MPCs are tracked across tens of wavelengths to examine small-scale statistics in massive MIMO systems. The others are based on large-scale variations in high-speed mobile communications. In [26], GPS delay information from an unmanned aerial vehicle at 900 MHz was exploited for tracking; while only a very small bandwidth of 10 MHz was available, because the airplane-to-ground distances are so huge, 30 m resolution was sufficient to discriminate between scatterers. In [27] and [28], MPCs were tracked in vehicular communications at 5.7 GHz with 1 GHz bandwidth using both the delay and path gain. Reference [29] also deals with tracking in vehicular communications, but at 3.4 GHz and with a 100 MHz bandwidth, incorporating linear arrays so that AoD and AoA could be estimated to obtain better discrimination. Finally, in [30], path gain, delay, and AoA—the latter provided through a virtual array, i.e., a single element moving on a train with known velocity—were used to track scatterers.

To recover from much greater path loss at mmWave frequencies compared to sub-6 GHz bands, antennas with very high

Manuscript received January 25, 2018; revised August 30, 2018; accepted December 11, 2018. Date of publication December 19, 2018; date of current version March 5, 2019. *(Corresponding author: Camillo Gentile.)*

C. Lai, C. Gentile, and J. Wang are with the Communications Technology Laboratory, National Institute of Standards and Technology, Gaithersburg, MD 20899 USA (e-mail: chiehping.lai@nist.gov; camillo.gentile@nist.gov; jian.wang@nist.gov).

R. Sun is with CableLabs, Louisville, CO 80027 USA (e-mail: ruoyusun@ieee.org).

P. B. Papazian and J. Senic are with the Communications Technology Laboratory, National Institute of Standards and Technology, Boulder, CO 80305 USA (e-mail: peter.papazian@nist.gov; jelena.senic@nist.gov).

Color versions of one or more of the figures in this paper are available online at http://ieeexplore.ieee.org.

Digital Object Identifier 10.1109/TAP.2018.2888686

gain (25–40 dBi), in turn, very narrowbeam (3°–12°), are necessary for transceivers to operate at reasonable distances: hundreds of meters outdoors in line-of-sight (LOS) conditions and tens of meters indoors in nonline-of-sight (NLOS). To provide omnidirectional coverage, the narrow beams must be steered toward the double-directional angles of the multipath in the environment. In LOS, this will be the direct path, the strongest available. However, when blocked—say by human bodies that severely attenuate the signal or in NLOS, given that wall materials have much higher penetration losses at mmWave frequencies [31]–the beam must be redirected toward other available paths to sustain connectivity.

In mobile environments, the AoD and AoA of the multipath will change as the TX and RX move. Because the beamwidths are so narrow, misalignment of just a few degrees may incur an additional loss in the link budget of up to 30 dB. Hence, equally essential for the link to operate is that the steerable beams can track the paths as they move about the environment. Even if a beam maintains perfect alignment with a path, path loss will change due to different path lengths and incident angles as the beam traverses a scattering surface; especially in the case of a room wall, for example, often with varying sections of wall materials and wall depths due to recessed doors, panels, and so on. Thus, multipath tracking takes on another functionality at mmWave.

To the best of our knowledge, only two papers—both published within the last year—deal with multipath tracking for channel modeling over 6 GHz. In [32], persistent paths are tracked across seven large-scale RX positions up to a range of 35 m from a fixed TX in LOS outdoors; using 1 GHz bandwidth, path gain, delay, and AoA are used to discriminate paths. The other paper [33] tracks MPCs indoors over a total of 150 positions in a large empty hall at 11 GHz with 400 MHz bandwidth; circular arrays at the TX and RX permit estimating the double-directional angles of the MPCs.

In this paper, we present a novel algorithm to track MPCs in a lecture room at 60 GHz. Tracking indoors is much more challenging because the scatterers are much closer together. As such, our work is most similar to [33], but we operate at a much higher center frequency than 11 GHz, rendering the problem much more demanding due to much higher path loss. The three main contributions of our work are as follows.

1) First to track MPCs with real 60 GHz channel measurements. Our state-of-the-art 3-D (azimuth and elevation) double-directional (AoD and AoA) channel sounder has 0.5 ns delay resolution and 2° average angle error to guarantee high-measurement fidelity. Due to the system's fast and autonomous data collection, channel acquisitions at 325 unique large-scale TX–RX configurations were recorded and for each eight small-scale measurements.
2) A novel algorithm for tracking MPCs based on the Assignment Problem, demonstrated robust enough to track distinct reflections 12 m across the surface of a wall composed from various materials and wall depths.
3) Parameters reduced from measurements to fit the quasi-deterministic (QD) channel model, a stochastic map-based model that was recently adopted by the IEEE 802.11ay task group. The stochastic model describes the dispersion characteristics of the channel in the multidimensional MPC space, allowing complete reconstruction of the directional channel impulse response. In particular, the model captures the variability in the parameters during tracking. It also captures the small-scale structure of the diffuse MPC power. We show the diffuse power to be up 40% of the total power.

The rest of this paper is organized as follows: In Section II, we provide the details of our channel sounder and of the measurement campaign. Section III describes the QD channel model and our methodology to reduce its parameters from the measurements. Section IV describes our novel tracking algorithm based on the Assignment Problem and Section V our tracking results, including the reduced model parameters. Section VI is reserved for the conclusion.

II. Channel Measurements

A. Channel Sounder

Fig. 1 displays the TX and RX of our 60 GHz channel sounder. The TX was mounted on a tripod at 2.5 m, while the RX was mounted on the mobile robot at 1.6 m. The TX features a semicircular array of eight horn antennas, each with 18.1 dBi gain and 22.5° beamwidth. In order to avoid "blind spots," the angular spacing between the elements was matched to the beamwidth of the horns. Specifically, the elements are spaced at 22.5° horizontally; vertically, adjacent elements are pointed outwards at 0°, and downward at 22.5° toward the RX. Consequently, the horizontal field of view (FOV) of the array is 180° and its vertical FOV is 45°. The 3-D spatial diversity enables characterizing AoD in both azimuth and elevation. The RX features two semicircular arrays to estimate AoA—each one is a replica of the TX array—extending the horizontal FOV of the array to omnidirectional. The omni view at the RX is essential because the RX is mobile, whereas the TX was fixed against a wall—typical for hot-spot deployments—hence emission from the backside was less important. The only other difference from the TX array is that the vertical elements are pointed upward at 22.5° toward the TX rather than downward.

The system generates a repeating 2047 bit pseudorandom (PN) code word that has a chip rate of 2 GHz. With 0.5 ps synchronization through Rubidium clocks, the signal is transmitted from a single TX element while the received signal is sequentially switched through the RX elements every two code words.[1] After a full RX cycle, the TX element is then also switched. Thus, a channel acquisition consisting of a full sweep of the 128 (8×16) pairs requires 262 μs. The code word is generated at IF and then upconverted to an RF center frequency of $f_c = 60.5$ GHz. At the RX, the received signal is downconverted back to IF and then digitized at 40 G samples/s. Oversampling both reduces aliasing and improves the signal-to-noise ratio [34]. For each pair, the received signal is correlated with the known PN code

[1]The extra code word is used to buffer the electronic switching time.

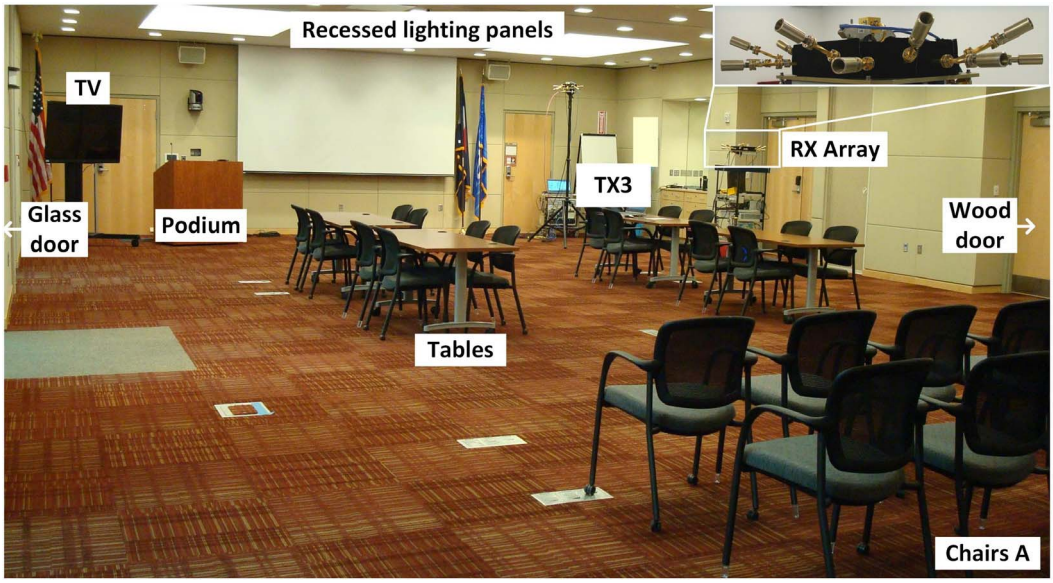

Fig. 1. 60 GHz channel sounder. The TX array is mounted on a tripod at 2.5 m, while the RX array is mounted on a mobile robot at 1.6 m. The inset of the RX array shows more detail.

word to generate a complex channel impulse response. The maximum measurable path loss of the system is 162.2 dB.

Given the antenna centers of the TX- and RX-array elements, the 128 channel impulse responses from a channel acquisition were coherently combined through the SAGE algorithm [35] to extract the channel MPCs. Any measurement taken with a channel sounder will contain not only the response of the channel but also the response of the sounder itself, namely, the directional patterns of the antennas and the responses of the TX and RX front ends. While the SAGE algorithm automatically deembeds the antenna patterns, the effects of the TX and RX front ends were removed through predistortion filters designed from a back-to-back calibration method [36]. Hence, the properties of the MPCs reflect the pure response of the channel alone and not that of the measurement system.

B. Measurement Campaign

The measurement campaign was conducted in a 19 m $\times$ 10 m lecture room. The laser-guided navigational system of the robot reported its position, heading, and speed at each RX position. It also generated a 2-D map of the environment—pictured in Fig. 2(a)—with centimeter accuracy. The top section of the room was occupied by four tables with surrounding chairs, while the bottom section by two rows of chairs. Other large objects in the room were a TV and podium in the top left corner of the room (shown in Fig. 1) and another TV at the bottom right. A projector screen was rolled down, covering a larger portion of the top wall. The doors on the left side were external glass doors, while the doors on the right side were made of wood and closed during measurements.

In our campaign, there were four TX positions, labeled as TX1–TX4. For each one, the receiver followed a trajectory demarcated by four waypoints, effectively forming a loop. LOS conditions were in effect throughout. While the waypoints were the same for all TXs, the number of actual RX positions collected per transmitter varied between 60 and 108. This is because the distance between RX positions depends on the time required to download the data collected at each one, which is variable based on the register space. For TX1, the 108 RX positions were marked by Xs in Fig. 2(a).

III. Quasi-Deterministic Channel Model

The IEEE 802.11ay task group [37] as well as other industry consortia [5] have subscribed to map-based channel models for mmWave systems, of which the QD model [38] has become the benchmark. In the QD model, only the direct path and reflected paths are considered as diffraction has been demonstrated to be much weaker in mmWave bands [31]. The direct path is completely deterministic: its geometrical properties (delay, AoD, and AoA) are computed from the TX and RX coordinates and its path loss from the Friis transmission equation in LOS. Specular reflections are also deterministic: their geometrical properties are computed from raytracing (provided a map of the environment in addition to the TX and RX coordinates) and their path loss is the sum of the free-space loss plus any reflection loss. Each specular reflection gives rise to scattering of the incident wave into a dominant specular MPC (a.k.a. cursor) and weaker diffuse components clustered around the cursor. The stochastic property of the model concerns the small-scale statistics of the clustered scattering. In this section, we describe the QD parameters such as the reflection loss of the cursors and the angular spread of the clusters—through which a complete channel realization can be generated—and our approach to extracting these parameters from the measurements.

A. MPC Clustering and QD-Parameter Fitting

From SAGE, the MPCs extracted from a channel acquisition were indexed by path gain (PG), delay (τ), and AoD and AoA

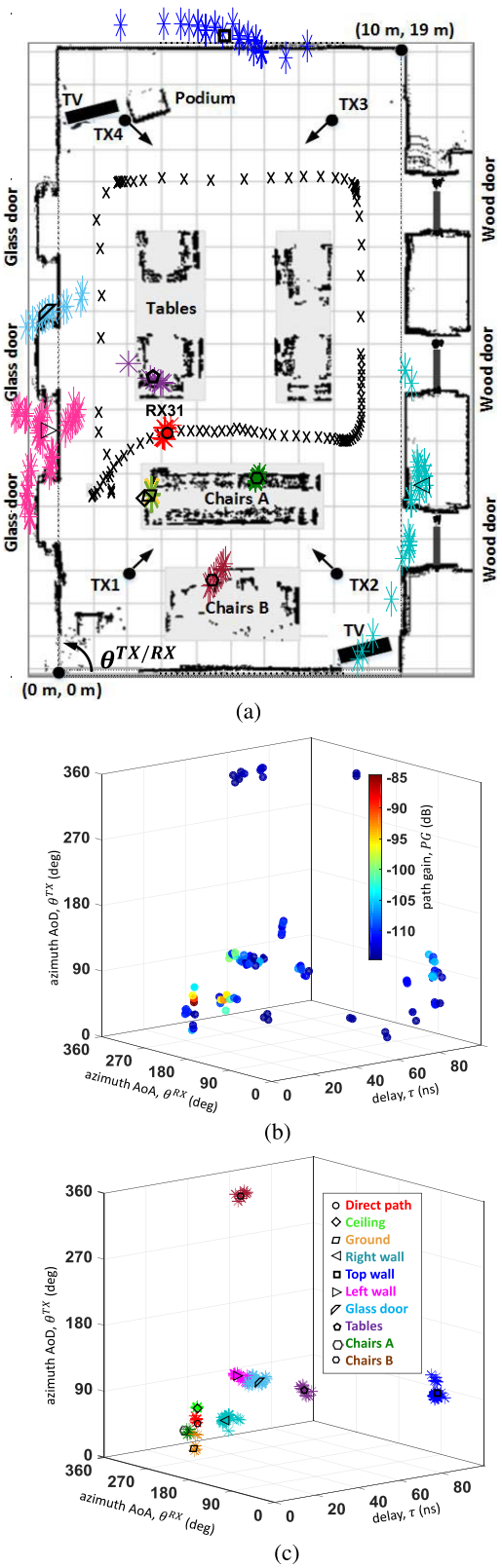

Fig. 2. (a) 2-D map of lecture room. The grid size is 1 m × 1 m. Labeled are TX1–TX4, and the RX positions for TX1 are marked with an X. For TX1–RX31, the clusters classified in Fig. 2(c) were transformed from the delay-angle space onto the map, keeping the same legend. (b) MPCs extracted from channel acquisition for illustrative configurattion TX1–RX31. Each MPC is indexed according to delay and azimuth AoD and AoA (elevation AoD and AoA are omitted) and coded against path gain in the color bar. (c) Clustering of MPCs from Fig. 2(b). Each cluster is color-coded against the reflector in the environment that generated it; also, each cluster cursor is highlighted with a black symbol.

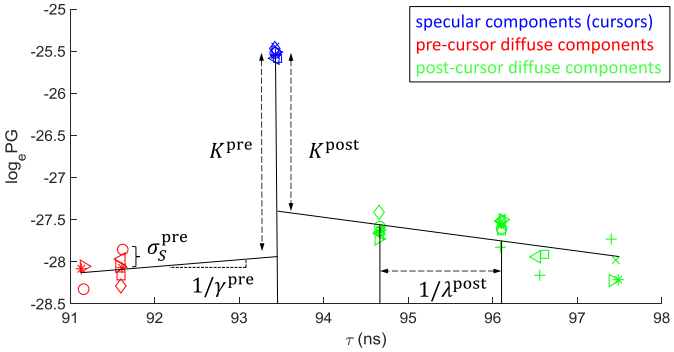

Fig. 3. Measured MPCs of a typical cluster aggregated over eight small-scale channel acquisitions (each acquisition is displayed with a different symbol). Note that the ordinate was plotted as $\log_e$ PG, converting (4) from exponential to linear form.

in azimuth $(\theta^{TX}, \theta^{RX})$ and in elevation (ϕ^{TX}, ϕ^{RX}), what we refer to as the MPC space. (The azimuth and elevation of the AoA and AoD were validated with a mean error of 2.1° [36].) As an illustrative example, Fig. 2(b) shows the MPCs for TX1–RX31. Once extracted, the paths were clustered in space through our mmWave-specific clustering algorithm in [39]. An underlying principle of the algorithm is that each cluster has a single peak originating from a specular reflection. Fig. 2(c) shows the clustering of the MPCs from Fig. 2(b); for each, the cursor identified is outlined with a distinct symbol.

Following the clustering step, the QD parameters of each cluster were fit to the data. Each cluster identified had N MPCs indexed through i. First, the azimuth root mean square (RMS) angle spreads were calculated as

$$\sigma_\theta^{TX/RX} = \sqrt{\frac{\sum_{i=1}^{N} PG_i \cdot \left(\theta_i^{TX/RX} - \mu_\theta\right)^2}{\sum_{i=1}^{N} PG_i}}$$
$$\mu_\theta = \frac{\sum_{i=1}^{N} PG_i \cdot \theta_i^{TX/RX}}{\sum_{i=1}^{N} PG_i}. \quad (1)$$

The elevation spreads were computed equivalently, substituting θ for ϕ.

Next, for each cluster, the cursor is identified as the MPC with the highest path gain, PG_{cursor}. The cursor path gain is given by the free-space gain, PG_{FS}, multiplied by the reflection gain, RG, due to incidence of the plane wave with the reflector, or $PG_{\text{cursor}} = PG_{\text{FS}} \cdot RG$. Given the delay of the cursor, τ_{cursor}, the free-space gain is known through the Friis transmission equation as $PG_{\text{FS}} = (1/4\pi f_c \tau_{\text{cursor}})^2$. Substituting the latter, then the reflection loss of the cursor is calculated as

$$RL = \frac{1}{RG} = \frac{1}{PG_{\text{cursor}} \cdot (4\pi f_c \tau_{\text{cursor}})^2}. \quad (2)$$

With the cursor identified, the remaining components within the cluster—considered diffuse components—were partitioned along the delay dimension into two sections: N_{pre} precursor MPCs arriving before the cursor and N_{post} postcursor MPCs arriving after, where $N = N_{\text{pre}} + N_{\text{post}} + 1$. Fig. 3 shows the measured MPCs for a typical cluster. The relative strength

of the cursor with respect to precursor or postcursor diffuse components is gaged through the Ricean K-factor as

$$K_{\text{pre/post}} = \frac{PG_{\text{cursor}}}{\sum_{i=1}^{N_{\text{pre/post}}} PG_i}. \tag{3}$$

The prediffuse and postdiffuse components then rise and fall according to

$$\begin{aligned} PG_{\text{pre}}(\tau) &= \frac{PG_{\text{cursor}}}{K_{\text{pre}}} e^{\frac{(\tau-\tau_{\text{cursor}})}{\gamma_{\text{pre}}}} + S_{\text{pre}} \\ PG_{\text{post}}(\tau) &= \frac{PG_{\text{cursor}}}{K_{\text{post}}} e^{-\frac{(\tau-\tau_{\text{cursor}})}{\gamma_{\text{post}}}} + S_{\text{post}} \end{aligned} \tag{4}$$

where γ is known as the decay constant determined through a least-squares fit to the extracted MPCs and $S \sim \mathcal{N}(0, \sigma_S)$ is the residual error. Finally, intracluster MPC arrivals are characterized as a Poisson process in which the interarrival intervals follow an exponential distribution function

$$f_{\text{post/pre}}(\tau_i|\tau_{i-1}) \sim \lambda_{\text{post/pre}} e^{-\lambda_{\text{post/pre}}(\tau_i-\tau_{i-1})} \tag{5}$$

where λ is known as the arrival rate.

Often clusters from a single acquisition contained only a few diffuse components, not enough for robust statistical characterization. That is why, for MPC clustering and QD-parameter fitting, we actually aggregated MPCs from the eight small-scale acquisitions. Because they were taken a wavelength apart, the scattering is known to be independent. Fig. 3 displays the eight measurements.

B. Cluster Classification

The clustered MPCs were transformed from the multidimensional delay-angle space to the coordinate system of the 2-D map through the raytracing equations in [10]. Fig. 2(a) shows the transformation from Fig. 2(c) for illustrative configuration TX1–RX31, keeping the same scheme as in the color bar. The azimuth coordinate system $\theta^{TX/RX}$ is also shown in the map. For the direct path, the coordinates correspond to the estimated position of the receiver (RX31 is labeled on the map for convenience), while for the first-order reflections, they correspond to the estimated reflection points. Although second-order reflections were also observed, they were omitted to reduce visual clutter. From the reflection points, the reflectors that generated each cluster could be classified. The cursors, indicated by distinct symbols in the legend, show the locations of the specular reflections while the others are dismissed as diffuse reflections. Note that the diffuse reflections could be spread quite far apart. While the most reflection points lied within 0.5 m of the reflectors classified, the location errors around the glass door were a bit higher due to the complex scattering environment around the metal door frame and handle, making path resolution difficult. Hence, a few points were transformed outside the room.

IV. Multipath-Component Tracking

In this section, we describe how cursors identified across consecutive RX positions are tracked. Over a long sequence of positions—as is the case with our campaign containing up to 108 positions per TX, over which the robot traverses a total distance of 33 m—the MPC properties of a cursor associated with the specific path (direct path and reflection from right wall) may vary widely. For example, we observed a cursor's path gain to vary up to 17 dB, its delay up to 45 ns, and its azimuth AoA angle up to degrees 80°. Because the properties vary so widely per cursor—moreover because there are multiple cursors over the sequence—different cursors can exhibit very similar properties in one or more dimensions of the MPC space, making discrimination difficult. In addition, cursors are subject to measurement error and clustering misclassification. Other issues that arise are that specular reflections may experience blockage, be interfered by a corner diffraction between contiguous reflection planes, or fall below the system noise floor. All these issues render tracking multiple cursors with real measurements a challenge.

A. Assignment Problem

To deal with this challenge, we pose cursor tracking in the framework of the Assignment Problem. The problem has been applied successfully in the field of computer vision for object tracking over a sequence of images in which similar issues occur, i.e., objects appear similar to or blocked by other objects in the scene [40]. Finding the best match between cursors at two consecutive positions by simply minimizing their distance in the MPC space, as in [21], [34], and [35], could yield two cursors at one position matched to a single cursor at the next position or vice versa. Rather, the Assignment Problem finds the best one-to-one correspondence that minimizes the distances between all possible cursor pairings collectively. This renders the tracking algorithm robust to the aforementioned issues.

Let RX position indexed through k has M_k cursors identified from the clustering stage. The cursors are indexed in the MPC space through $j_k = 1 \ldots M_k$ as

$$\boldsymbol{x}_{j_k} = \left\{PG_{j_k}, \tau_{j_k}, \theta_{j_k}^{TX}, \phi_{j_k}^{TX}, \theta_{j_k}^{RX}, \phi_{j_k}^{RX}\right\}. \tag{6}$$

The distance along dimension l, $l = 1 \ldots 6$, in the space between any cursor j_k at position k and any other cursor j_{k+1} at the consecutive position is defined as

$$\Delta \boldsymbol{x}^l_{j_k, j_{k+1}} = \left| x^l_{j_k} - x^l_{j_{k+1}} \right|. \tag{7}$$

To account for different units and range of values across the six dimensions, the distance along each dimension is normalized by the minimum and maximum values observed between the two positions. The normalized values are then combined across all dimensions to formulate a single cost, $c_{j_k, j_{k+1}}$, between the two cursors

$$c_{j_k, j_{k+1}} = \sum_{l=1}^{6} \frac{\Delta x^l_{j_k, j_{k+1}} - \min\limits_{j_k, j_{k+1}} \Delta x^l_{j_k, j_{k+1}}}{\min\limits_{j_k, j_{k+1}} \Delta x^l_{j_k, j_{k+1}} - \min\limits_{j_k, j_{k+1}} \Delta x^l_{j_k, j_{k+1}}}. \tag{8}$$

With the cost values in hand, the Assignment Problem can be expressed precisely as an integer programming problem

$$\begin{aligned}
&\min \sum_{j_k=1}^{M_k} \sum_{j_{k+1}=1}^{M_{k+1}} c_{j_k,j_{k+1}} \cdot a_{j_k,j_{k+1}} \\
&\text{s.t.} \sum_{j_{k+1}=1}^{M_{k+1}} a_{j_k,j_{k+1}} = 1, \quad \forall j_k = 1 \ldots M_k, \text{ if } M_k < M_{k+1} \\
&\quad \sum_{j_k=1}^{M_k} a_{j_k,j_{k+1}} = 1, \quad \forall j_{k+1} = 1 \ldots M_{k+1}, \text{ if } M_k \geq M_{k+1} \\
&\quad a_{j_k,j_{k+1}} \in \{0, 1\} \qquad (9)
\end{aligned}$$

for which the variable $a_{j_k,j_{k+1}} = 1$ if there is a match between cursors j_k and j_{k+1} and 0 otherwise. This formulation accounts for the birth–death process in channel modeling [3] in which cursors either are "born" between positions ($M_k < M_{k+1}$) or alternatively "die" or their number remains unchanged ($M_k \geq M_{k+1}$). The integer program is solved for all pairs of consecutive positions through the Hungarian algorithm [41].

B. Iterative Tracking

By virtue of the birth–death process, some cursors will be matched across a long segment of consecutive positions, forming a track. A track is spurred by cursors that are well separated in space from other cursors over the segment and so can be matched unambiguously. Conversely, there will be other cursors matched across only a few positions—or not matched at all—that cannot be reliably assigned to a track due to measurement error, crowding of cursors in space, blockage, and so on. To enhance their discrimination, we implement an iterative tracking algorithm. Through iteration, indiscriminate cursors are "pulled" toward neighboring tracks. In the sequel, the iterative algorithm is explained in detail.

An empirical threshold of seven positions (across six consecutive matches) is used to designate whether the segment is long enough to be considered a track. For track T, a spline—a linear polynomial defined piecewise in the multidimensional MPC space—denoted as $S(\boldsymbol{x}; \boldsymbol{x}_{j_{\tilde{k}}} \in T)$ is fit through regression to all cursors on the track, $\boldsymbol{x}_{j_{\tilde{k}}}$, where $\tilde{k}$ indexes the segment over which the track is defined. The function of the spline is to smooth over measurement errors, and, by using robust regression, measurement outliers are excluded. The problem is that smoothing depends on the cursors assigned to a track; if the assignment is wrong, then smoothing will not reduce the error. That is why we adopt an iterative approach, iterating between assignment and smoothing.

Specifically, after the spline fitting, the cursors on the tracks are smoothed as

$$\boldsymbol{x}_{j_k}^{m+1} = (1 - \alpha^m) \cdot \boldsymbol{x}_{j_k}^{m} + \alpha^m S\left(\boldsymbol{x}_{j_k}^{m}; \boldsymbol{x}_{j_{\tilde{k}}}^{m} \in T^m\right) \qquad (10)$$

where m is the iteration index and the initial conditions are $\boldsymbol{x}_{j_k}^{0} = \boldsymbol{x}_{j_k}$. The smoothed cursor, $\boldsymbol{x}_{j_k}^{m+1}$, will lie between $\boldsymbol{x}_{j_k}^{m}$ and the projection of $\boldsymbol{x}_{j_k}^{m}$ onto the spline, $S(\boldsymbol{x}_{j_k}^{m}; \boldsymbol{x}_{j_{\tilde{k}}}^{m} \in T^m)$. Where the smoothed cursor lies precisely depends on the learning parameter, α^m. The parameter is initialized to $\alpha^0 = 0$, for which all weight is allocated to the measurements. At each iteration, α^m is increased by some $\Delta\alpha$, shifting more weight to the projected cursors.

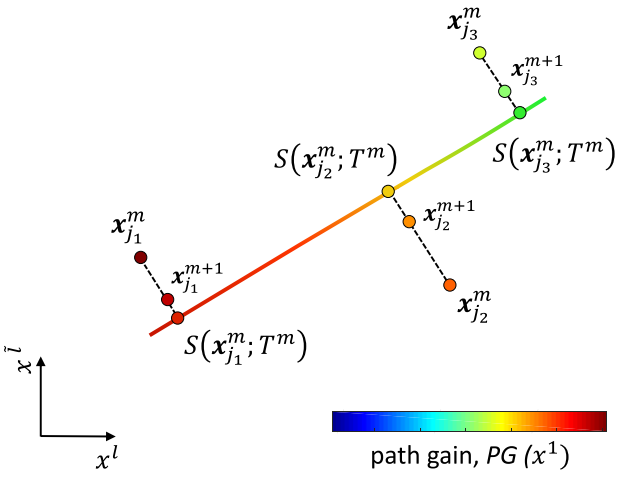

Fig. 4. Figurative example of cursors in space, $\boldsymbol{x}_{j_1}^m$, $\boldsymbol{x}_{j_2}^m$, and $\boldsymbol{x}_{j_3}^m$, identified as part of the same track, T^m, at iteration m and so fit to the spline shown. Also, their projections, $S(\boldsymbol{x}_{j_1}^m; T^m)$, $S(\boldsymbol{x}_{j_2}^m; T^m)$, and $S(\boldsymbol{x}_{j_3}^m; T^m)$ are shown onto the spline and the smoothed cursors, $\boldsymbol{x}_{j_1}^{m+1}$, $\boldsymbol{x}_{j_2}^{m+1}$, and $\boldsymbol{x}_{j_3}^{m+1}$.

A figurative example is displayed in Fig. 4. Three cursors in space, $\boldsymbol{x}_{j_1}^m$, $\boldsymbol{x}_{j_2}^m$, and $\boldsymbol{x}_{j_3}^m$ are shown in Fig. 4. They are all identified as part of track T^m at iteration m and so fit to $S(\boldsymbol{x}; \boldsymbol{x}_{j_1}^m, \boldsymbol{x}_{j_2}^m, \boldsymbol{x}_{j_3}^m \in T^m)$. Also, their projections, $S(\boldsymbol{x}_{j_1}^m; \boldsymbol{x}_{j_1}^m, \boldsymbol{x}_{j_2}^m, \boldsymbol{x}_{j_3}^m \in T^m)$, $S(\boldsymbol{x}_{j_2}^m; \boldsymbol{x}_{j_1}^m, \boldsymbol{x}_{j_2}^m, \boldsymbol{x}_{j_3}^m \in T^m)$, and $S(\boldsymbol{x}_{j_3}^m; \boldsymbol{x}_{j_1}^m, \boldsymbol{x}_{j_2}^m, \boldsymbol{x}_{j_3}^m \in T^m)$ onto the spline are also shown in Fig. 4. In this example, $\alpha^m = 0.7$ and so the smoothed cursors, $\boldsymbol{x}_{j_1}^{m+1}$, $\boldsymbol{x}_{j_2}^{m+1}$, and $\boldsymbol{x}_{j_3}^{m+1}$ are closer to the projected cursors than to $\boldsymbol{x}_{j_1}^m$, $\boldsymbol{x}_{j_2}^m$, and $\boldsymbol{x}_{j_3}^m$, respectively.

Once the cursors have been smoothed at iteration m, in the next iteration $\boldsymbol{x}_{j_k}^{m+1}$ is substituted for $\boldsymbol{x}_{j_k}$ in (7)–(9) and the cursors are smoothed once more through (10); so on and so forth. Iterations continue until convergence at $\alpha^m \geq 1$, at which the measured cursors bear no weight and smoothed cursors all lie on one of the splines. A flowchart of the iterative tracking algorithm appears in Fig. 5. By solving the Assignment Problem with smoothed cursors, cursors are effectively exchanged between tracks and the splines are modified accordingly. Indiscriminate cursors close to multiple splines will fluctuate between them throughout the iterations and eventually merge with the ones that provide the best fit.

V. Results

In this section, we present the parameters of the QD model reduced from our measurement campaign. To date, others have provided the model parameters from their measurements campaigns per environment. Hence, the values reported were averaged over all cluster-generating reflectors in the environment. In reality, different reflectors may have very different scattering properties and so should be reported per reflector. This is a novelty of our work. Also to date, only the mean values of the parameters have been provided. Rather, here we provide in addition their standard deviation, which enables

TABLE I

PARAMETERS OF THE QD CHANNEL MODEL FOR SINGLE-ORDER REFLECTORS IDENTIFIED FOR EACH TRANSMITTER

Transmitter			TX1				TX2				TX3				TX4			
Reflector			Right wall	Ceil.	Top wall	Tables	Right wall	Ceil.	Top wall	Left wall	Right wall	Ceil.	Left wall	Bott. wall	Right wall	Ceil.	Top wall	Bott. wall
Ricean K-factor, K (dB)	pre	μ		6.20	5.69				5.03	5.42				3.10				
		σ		3.20	2.97				1.68	1.68				1.50				
	post	μ	4.00	7.37	4.67	4.28	5.31	10.3	5.07	7.33	7.40	9.60	5.60	7.61	4.60	6.29	5.16	5.90
		σ	2.08	2.78	2.44	1.71	2.58	2.17	2.65	3.15	2.54	1.36	2.92	2.26	2.40	2.18	2.69	2.70
decay constant, γ (ns)	pre	μ		1.44	0.28				0.73	1.39				0.91				
		σ		0.64	0.14				0.14	0.71				0.25				
	post	μ	1.08	1.60	1.58	0.77	0.77	1.42	1.63	1.50	1.21	0.41	0.61	0.78	0.71	1.52	0.93	0.86
		σ	0.56	0.83	0.61	0.38	0.40	0.70	0.69	0.78	0.58	0.01	0.31	0.32	0.37	0.79	0.45	0.44
standard deviation residual fit error, σ_S (dB)	pre	μ		1.03	1.72				1.67	1.63				2.41				
		σ		0.30	0.86				0.86	0.86				1.25				
	post	μ	3.10	3.53	1.29	2.80	1.89	2.92	1.33	1.89	2.19	0.73	2.02	1.20	1.38	2.06	1.25	2.02
		σ	1.25	0.95	0.60	1.42	0.99	1.51	0.39	0.60	0.65	0.34	0.99	0.39	0.73	0.90	0.52	0.99
arrival rate, λ (1/ns)	pre	μ		0.84	1.41				0.89	1.04				0.94				
		σ		0.20	0.74				0.20	0.33				0.29				
	post	μ	1.08	0.78	0.95	0.81	1.38	0.84	1.62	1.14	0.82	0.58	1.37	1.53	1.29	0.55	1.50	1.68
		σ	0.39	0.15	0.35	0.01	0.37	0.26	0.72	0.56	0.18	0.01	0.53	0.55	0.67	0.28	0.72	0.88
angle spread, $\sigma^{TX/RX}$ (deg)	θ	μ	3.56	2.09	3.10	4.42	2.63	2.10	2.75	2.64	2.56	2.36	3.44	2.65	1.98	3.4	1.57	2.17
		σ	1.23	1.09	1.62	2.31	1.37	1.09	1.43	1.38	1.27	1.23	1.56	1.31	1.03	1.78	0.50	0.99
	ϕ	μ	3.53	2.93	3.46	5.01	3.46	3.54	2.31	3.39	3.37	3.97	3.30	3.13	3.31	4.89	3.02	2.19
		σ	1.72	1.53	1.59	2.30	1.81	1.85	1.07	1.65	1.18	1.55	1.43	1.63	1.68	2.55	0.97	0.66
reflection loss, RL (dB)		μ	10.80	6.90	9.27	6.58	9.80	6.20	10.23	10.70	7.52	5.01	9.84	9.67	10.39	7.17	10.49	9.63
		σ	4.24	2.69	5.70	3.00	2.64	3.40	2.31	3.00	1.33	2.5	1.52	4.00	3.20	0.90	1.07	1.66

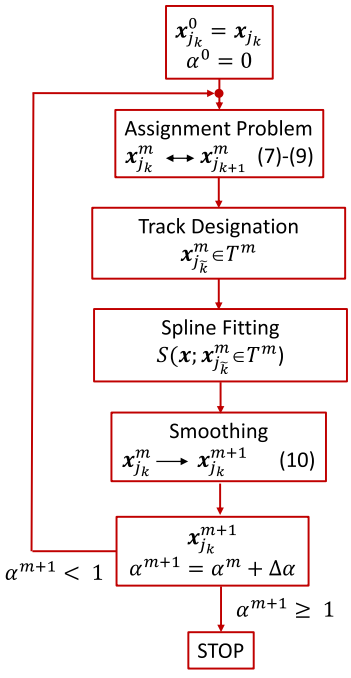

Fig. 5. Flowchart of iterative tracking algorithm.

modeling the variation in the cluster properties as the cursor is tracked, critical to the proper design of beam-tracking algorithms for mmWave systems.

The model parameters [(1)–(5)] are reported in Table I. The reflectors are divided by the TX position. Indeed, the reflectors in the environment are the same for all TXs; however, what the transmitter can "see" depends on its orientation given its limited 180° horizontal FOV. This means that each TX may detect the same top, bottom, left, and right walls, but different segments of it. While the QD parameters can certainly be combined over the four TX positions, we preferred to present them separately for the sake of comparison. For illustrative purposes, we concentrate on TX1 in Section V-A and then consider other parameters across all transmitters in Section V-B.

A. TX1

Fig. 6(a) displays the cursors tracked in the MPC space across the 108 RX positions for TX1. Each track cursor is indicated by a symbol according to the corresponding reflector in the legend and is also coded against path gain in the color bar. While the cursors for the direct path and right-wall reflections were detected across all positions ($k = 1 \ldots 108$), other reflections were too weak to be detected at some. As such, individual tracks are labeled by their beginning and end positions. In Fig. 6(b), the tracks in Fig. 6(a) were transformed from the delay-angle space onto the 2-D map, as explained in Section III-B. The same color scheme, symbols, and position labeling were kept.

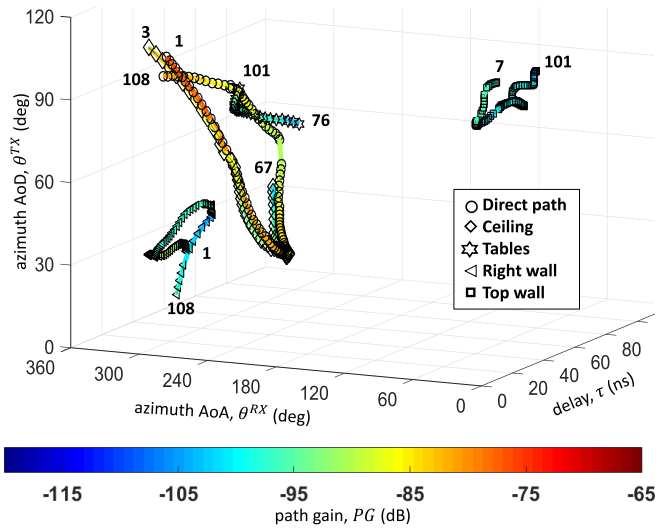

(a)

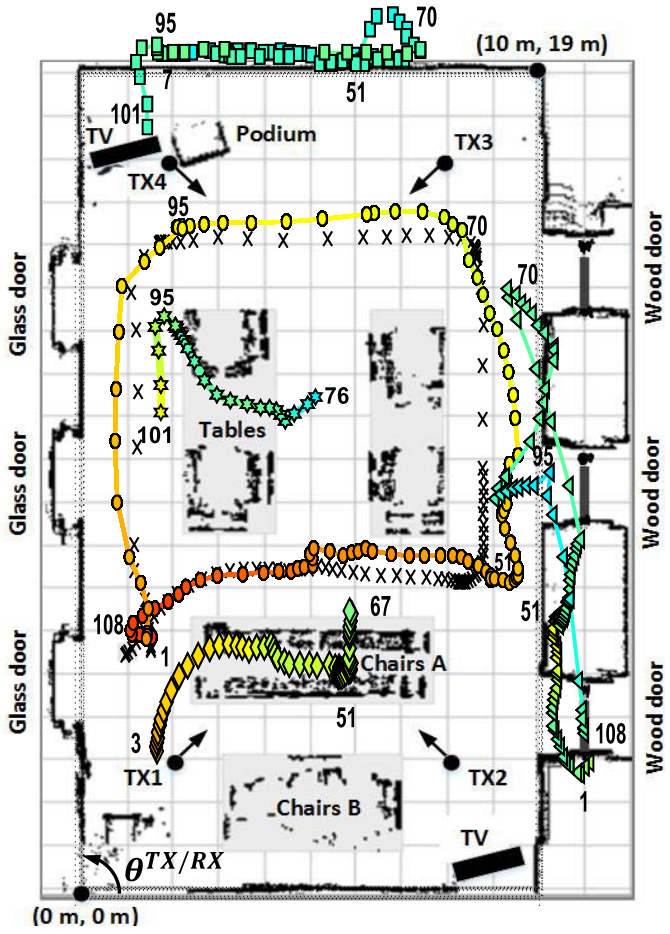

(b)

Fig. 6. (a) Cursors tracked in the MPC space across 108 RX positions for TX1. Each track cursor is indicated by a symbol according to the corresponding reflector in the legend and is also coded against path gain in the color bar. The beginning and end positions of each track are also labeled since most cursors are deteced across only a fraction of the positions. (b) Cursors tracked in the 2-D map of the environment—transformed from from the delay-angle space in Fig. 6(a)—across the 108 RX positions for TX1. The ground-truth RX positions are marked as Xs. The symbol legend and color bar from Fig. 6(a) are kept.

Consider first the direct path in Fig. 6(b), which lies along the ground-truth positions of the receiver—marked with Xs—as reported by the robot's navigational system. For the sake of reference, the three waypoints where the robot turns are also labeled on the track ($k = 51$, 70, and 95). One can observe that the path gain decreased as the robot moved farther from the TX and vice versa. In fact, the average path-gain deviation from the Friis transmission equation was 0.1 dB with a standard deviation of 1.52 dB. One can see that the estimated direct path follows the ground-truth direct path very well. Because there is no scattering associated with direct path, no QD parameters were reported for it.

Now consider the right-wall track. The three waypoints are also labeled on it. From $k = 1 \ldots 51$, the path gain increased continuously as the robot moved along the bottom segment of the loop until it achieved a maximum value of -97 dB around the first corner, where the path length was shortest. From there, the path gain continued to decrease as the robot rounded the second corner ($k = 70$), achieving a minimum value around the third corner ($k = 95$), where the path length was longest; it then started to increase again until the final position in the loop ($k = 108$). The walls of the lecture room are composed from fabric panels over sheetrock (see Fig. 1). A mean reflection loss of $\mu_{RL} = 10.4$ dB was witnessed. The reflection loss certainly varied due to the different incident angles as the signal traversed the wall at different RX positions. It also varied because the signal did not just traverse the right wall, but also the internal doors made from wood, resulting in a standard deviation of the reflection loss of $\sigma_{RL} = 4.2$ dB. Note that the mean and standard deviation of the RL were very consistent across TX2 and TX4 as well, with $\mu_{RL} = 10.6$ dB and $\mu_{RL} = 10.4$ dB, respectively. For TX3, the value dropped significantly to 7.4 dB because the track was much shorter than for the other three—only 15 positions—and so was focused on the area of a wall divider which is bare sheetrock. Due to longer path length and reflection loss, the right-wall track is weaker than the direct path for any given RX position. The smaller signal-to-noise ratio affects angle estimation, contributing to a large location error in the map: whereas the yellow segment of the track, where the signal was strongest, aligned almost perfectly with the wall, for the weakest cyan segment, where the robot was farthest away from the reflected path, the location error was up to a meter from the nominal position of the wall. Although the error was less than 50 cm along the wall proper (i.e., between the doors), the error increases around the doors because of the complex reflection environment within the recessed area and also due to the diffraction from the corners.

The behavior of the top-wall track was similar to the other two tracks described: the signal was strongest along the top segment of the robot loop, where the path length was shortest, weaker along the left and right segments, and weakest along the bottom segment, in particular, around TX1 where the RX was farthest from the reflected path. In theory, the ceiling bounce has the same azimuth angles as the direct path and a slightly longer delay. That is why the two appear wrapped

around each other in space in Fig. 6(a). The fact that they can be discriminated over such a long segment ($k = 3 \ldots 67$) attests to the robustness of the tracking algorithm. Due to their different elevation angles, they are well separated in the 2-D map in Fig. 6(b). The ceiling bounce was detected for most of the bottom and right segments of the loop—note the distinct knee in the track as the robot rounds the corner at $k = 51$—but lost track along the top segment where the receiver was farthest from TX1. Like the other reflections, the ceiling bounce has a longer path length than the direct path and its average reflection loss was $\mu_{RL} = 8.9$ dB. The counterpart ground bounce was also detected at many RX positions [see Fig. 2(a) and (c) for TX1—RX31], but not reliably enough to form a track; the ground bounce has as geometrical disadvantage in FOV compared to the ceiling bounce due to the transmitter being closer to the ceiling.

It is worth noting that reflections from other large objects in the environment were also detected, in particular, from the tables on the left side of the room from $k = 76 \ldots 101$, hence mostly along the top and left segments of the loop. The path gain increased as the RX moved closer to TX1 and the distinct knee in the track corresponds with the third corner of the loop ($k = 95$). The TV in the front of the room was also detected, but only over three consecutive positions, and the podium only over two; but because they did not constitute persistent tracks, they were not reported.

B. Other Parameters

The K-factor quantifies the ratio of the cursor power to the aggregate power of the prediffuse or postdiffuse components in the cluster. It is insightful to reformulate it as the ratio of the diffuse power to the total power as $((1/K^{\text{pre}})+(1/K^{\text{post}}))/(1+(1/K^{\text{pre}})+(1/K^{\text{post}}))$. Our findings show that the latter varied from 8.6% to 39.9% across all reflectors and transmitter positions, with an average value of 25.0%. This means that the diffuse components contributed a significant amount of power and so cannot be neglected when accuracy is paramount in the channel modeling. The total power was spread on average 2.7° in azimuth angle and came in slightly higher at 3.4° in elevation.

The properties of the precursors and postcursors sectors were comparable, except that the postcursor section was observed in all clusters, while the precursor section was observed in only five reflectors in Table I (the parameters are otherwise shaded in gray). This is consistent with other measurement campaigns [38]; however, the decay constants were smaller than what was observed at 60 GHz in [38]—indicating that the diffuse components died down faster—but in that citation, the measurements were taken outside. The residual error of the fit, σ_S, ranged in 0.7–3.6 dB, with an average value of 1.9 dB, meaning that the data matched the model structure well. Finally, we found our arrival rate to be about an order of magnitude than [38]. Besides a different environment, this also has to do with the system dynamic range and delay resolution. Our system has both much greater dynamic range and much greater resolution, increasing the number of rays that can be observed by the system, in turn, increasing the arrival rate.

VI. Conclusion

In this paper, we reported the results from an extensive channel-measurement campaign—including a total of 325 unique TX—RX configurations—with our state-of-the-art 3-D double-directional 60 GHz channel sounder in a lecture room. Because of the sheer mass of data collected, we introduced an end-to-end methodology for the automatic reduction of the measurement data to channel-model parameters, including unsupervised clustering and a novel MPC tracking algorithm based on the Assignment Problem. For each of the four transmitter positions investigated, we found that, besides the direct path, there were on average four other paths from first-order reflections that could be reliably exploited for spatial multiplexing. Over the secondary paths, the reflection loss varied between 5.0 and 10.8 dB, with an average loss of 8.7 dB. For each of these paths, the diffuse power was found to be between 8.6% and 39.9% of the total power. Dispersion characteristics were also reported per path, including the Ricean K-factor varying in the range of 3.1–10.3 dB, with an average value of 6.0 dB, and angular spreads varying in the range of 1.6° –5°, with an average value of 3.1°.

References

[1] A. A. M. Saleh and R. A. Valenzuela, "A statistical model for indoor multipath propagation," *IEEE J. Sel. Areas Commun.*, vol. JSAC-5, no. 2, pp. 128–137, Feb. 1987.

[2] H. Asplund, A. A. Glazunov, A. F. Molisch, K. I. Pedersen, and M. Steinbauer, "The COST 259 directional channel model—Part II: Macrocells," *IEEE Trans. Wireless Commun.*, vol. 5, no. 12, pp. 3434–3450, Dec. 2006.

[3] Y. D. Bultitude and T. Rautiainen, "IST-4-027756 winner II D1. 1.2 V1. 2 winner II channel models," EBITG, TUI, UOULU, CU/CRC, Nokia, Tech. Rep., 2007.

[4] L. Liu *et al.*, "The COST 2100 MIMO channel model," *IEEE Wireless Commun.*, vol. 19, no. 6, pp. 92–99, 2012.

[5] *METIS II Project Homepage*. Accessed: 2016. [Online]. Available: https://metis-ii.5g-ppp.eu/

[6] *MiWEBA Project Homepage*. Accessed: 2016. [Online]. Available: http://www.miweba.eu

[7] *mm MAGIC Project Homepage*. Accessed: 2017. [Online]. Available: https://5g-mmmagic.eu/

[8] *5G mmWave Channel Model Alliance*. Accessed: 2015. [Online]. Available: https://www.nist.gov/ctl/5g-mmwave-channel-model-alliance/

[9] *Study on Channel Model for Frequency Spectrum Above 6 GHz*, document 38.900, v14, 3GPP, Mar. 2017.

[10] G. D. Galdo, N. Czink, and M. Haardt, "Cluster spatial localization from high-resolution parameter estimation," in *Proc. ITG Workshop Smart Antennas*, 2006, pp. 1–7.

[11] A. J. Braga and C. Gentile, "An ultra-wideband radar system for through-the-wall imaging using a mobile robot," in *Proc. IEEE Int. Commun. Conf.*, Jun. 2009, pp. 1–6.

[12] C. Gentile, S. M. Lopez, and A. Kik, "A comprehensive spatial-temporal channel propagation model for the ultrawideband spectrum 2–8 GHz," *IEEE Trans. Antennas Propag.*, vol. 58, no. 6, pp. 2069–2077, Jun. 2010.

[13] M. Froehle, P. Meissner, and K. Witrisal, "Tracking of UWB multipath components using probability hypothesis density filters," in *Proc. IEEE Conf. Ultra-Wideband*, Sep. 2012, pp. 306–310.

[14] Z. E. Gu Gunawan, "Temporal smoothing for subspace tracking of multipath signals in fading channel," in *Proc. IEEE Conf. Acoustic, Speech, Signal Process.*, Apr. 2003, p. V-161.

[15] W. G. Diab and H. M. Elkamchouchi, "DOA tracking in multipath environment based on the direction lock loop," in *Proc. IEEE Conf. Signal Process. Commun.*, Nov. 2007, pp. 1099–1102.

[16] B. Y. Shikur, M. Farmani, and T. Weber, "TOA/AOA/AOD-based 3-D mobile terminal tracking in NLOS multipath environments," in *Proc. IEEE Workshop Positioning, Navigat., Commun.*, Mar. 2012, pp. 201–205.
[17] M. Zhou, J. J. Zhang, and A. Papandreou-Suppappola, "Probability hypothesis density filtering with multipath-to-measurement association for urban tracking," in *Proc. IEEE Conf. Acoust., Speech, Signal Process.*, Mar. 2012, pp. 3273–3276.
[18] L. Li and J. L. Krolik, "Target tracking in uncertain multipath environment using distributed angle-of-arrival observation," in *Proc. IEEE Radar Conf.*, May 2015, pp. 1473–1478.
[19] J. Maceraudi, F. Dehmas, B. Denis, and B. Uguen, "Multipath components tracking adapted to integrated IR-UWB receivers for improved indoor navigation," in *Proc. IEEE Eur. Signal Process. Conf.*, Aug. 2016, pp. 753–757.
[20] Q. Wang *et al.*, "A framework of automatic clustering and tracking for time-variant multipath components," *IEEE Commun. Lett.*, vol. 21, no. 24, pp. 953–956, Apr. 2017.
[21] C. Huang, R. He, Z. Zhong, Y.-A. Geng, Q. Li, and Z. Zhong, "A novel tracking-based multipath component clustering algorithm," *IEEE Antennas Wireless Propag. Lett.*, vol. 16, pp. 2679–2683, Aug. 2017.
[22] M. S. Grewal, A. P. Andrews, and R. W. Bass, "Kalman filtering: Theory and practice," *IEEE Trans. Autom. Control*, vol. 40, no. 11, p. 1983, 1995.
[23] D. Shutin and G. Kubin, "Tracking and prediction of multipath components in wireless MIMO channels," in *Proc. IEEE Veh. Technol. Conf. (VTC Spring)*, Apr. 2007, pp. 329–333.
[24] X. Gao, F. Tufvesson, and O. Edfors, "Massive MIMO channels—Measurements and models," in *Proc. IEEE Asilomar Conf. Syst., Signals, Comput.*, Nov. 2013, pp. 280–284.
[25] A. Mannesson, M. A. Yaqoob, and B. Bernhardsson, "Tightly coupled positioning and multipath radio channel tracking," *IEEE Trans. Aerosp. Electron. Syst.*, vol. 52, no. 4, pp. 1522–1535, Aug. 2016.
[26] N. Schneckburger and D. Shutin, "Sparse adaptive multipath tracking for low bandwidth ranging applications," in *Proc. IEEE Conf. Acoust., Speech, Signal Process.*, May 2014, pp. 6424–6428.
[27] P. Paschalidis, K. Mahler, A. Kortke, M. Peter, and W. Keusgen, "Statistical evaluation of multipath component lifetime in the car-to-car channel at urban street intersections based on geometrical tracking," in *Proc. IEEE Veh. Technol. Conf. (VTC Spring)*, May 2012, pp. 1–5.
[28] K. Mahler, W. Keusgen, F. Tufvesson, T. Zemen, and G. Caire, "Tracking of wideband multipath components in a vehicular communication scenario," *IEEE Trans. Veh. Technol.*, vol. 66, no. 1, pp. 15–25, Jan. 2017.
[29] K. Saito, K. Kitao, T. Imai, and Y. Okumura, "Dynamic MIMO channel modeling in urban environment using particle filtering," in *Proc. IEEE Eur. Conf. Antennas Propag.*, Apr. 2013, pp. 980–984.
[30] F. Luan, A. F. Molisch, L. Xiao, F. Tufvesson, and S. Zhou, "Geometrical cluster-based scatterer detection method with the movement of mobile terminal," in *Proc. IEEE Veh. Technol. Conf. (VTC Spring)*, May 2015, pp. 1–6.
[31] J. Senic, C. Gentile, P. B. Papazian, K. A. Remley, and J.-K. Choi, "Analysis of E-band path loss and propagation mechanisms in the indoor environment," *IEEE Trans. Antennas Propag.*, vol. 65, no. 12, pp. 6562–6573, Dec. 2017.
[32] B. N. Liya and D. G. Michelson, "Characterization of multipath persistence in device-to-device scenarios at 30 GHz," in *Proc. IEEE Global Commun. Conf.*, Dec. 2016, pp. 1–6.
[33] P. Hanpinitsak, K. Saito, J.-I. Takada, M. Kim, and L. Materum, "Multipath clustering and cluster tracking for geometry-based stochastic channel modeling," *IEEE Trans. Antennas Propag.*, vol. 65, no. 11, pp. 6015–6028, Nov. 2017.
[34] P. B. Papazian, C. Gentile, K. A. Remley, J. Senic, and N. Golmie, "A radio channel sounder for mobile millimeter-wave communications: System implementation and measurement assessment," *IEEE Trans. Microw. Theory Techn.*, vol. 64, no. 9, pp. 2924–2932, Aug. 2016.
[35] P. B. Papazian *et al.*, "Calibration of millimeter-wave channel sounders for super-resolution multipath component extraction," in *Proc. IEEE Eur. Conf. Antennas Propag.*, Apr. 2016, pp. 1–5.
[36] R. Sun *et al.*, "Design and calibration of a double-directional 60 GHz channel sounder for multipath component tracking," in *Proc. IEEE Eur. Conf. Antennas Propag.*, Mar. 2017, pp. 3336–3340.
[37] Accessed: 2017. [Online]. Available: http://www.ieee802.org/11/Reports/tgay_update.htm
[38] A. Maltsev *et al.*, "Quasi-deterministic approach to mmWave channel modeling in a non-stationary environment," in *Proc. IEEE GLOBECOM*, Dec. 2014, pp. 966–971.
[39] J. Wang, C. Gentile, J. Senic, R. Sun, P. B. Papazian, and C. Lai, "Unsupervised clustering for millimeter-wave channel propagation modeling," in *Proc. IEEE Veh. Technol. Conf. (VTC-Fall)*, Sep. 2017, pp. 1–4.
[40] C. Huang, B. Wu, and R. Nevatia, "Robust object tracking by hierarchical association of detection responses," in *Proc. Eur. Conf. Comput. Vis.*, 2008, pp. 788–801.
[41] M. S. Bazaraa, J. J. Jarvis, and H. D. Sherali, *Linear Programming and Network Flows*, 2nd ed. Hoboken, NJ, USA: Wiley, 1990.

Chiehping Lai received the B.S. degree in electrical engineering from National Chung Hsing University, Taichung, Taiwan, in 2000, and the M.S. and Ph.D. degrees in electrical engineering from Pennsylvania State University, University Park, PA, USA, in 2004 and 2007, respectively.

He is currently a Computer Engineer with the Communications Technology Laboratory, National institute of Statandards and Technology, Gaithersburg, MD, USA. His current research interests include millimeter-wave systems, tracking algorithms, and data processing.

Ruoyu Sun (M'13–SM'17) was born in Hohhot, China. He received the B.S. degree in electrical engineering from Tianjin University, Tianjin, China, in 2004, the M.S. degree in electrical engineering from Beijing Jiaotong University, Beijing, China, in 2007, and the Ph.D. degree in electrical engineering from the University of South Carolina, Columbia, SC, USA, in 2015.

From 2015 to 2018, he was an Electronics Engineer with the National Institute of Standards and Technology, Boulder CO, USA, where he was involved in millimeter-wave channel sounder design, channel measurements and modeling. From 2007 to 2010, he was a System Integration Test Engineer in TD-SCDMA/GSM/GRPS protocol and platforms with T3G Technology Co., Ltd, MOTOROLA, and ST-Ericsson, in China. He is currently a Lead Architect with CableLabs, Louisville, CO, USA. He has authored or co-authored over 50 articles, served on over 10 conference Technical Program Committees, and reviewed over 150 manuscripts for academic journals and conferences. His current research interests include radio propagation channel measurements and modeling.

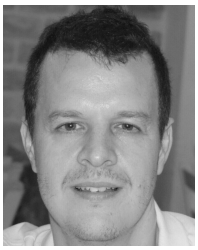

Camillo Gentile (M'01) received the joint B.S. and M.S. degrees in electrical engineering from Drexel University, Philadelphia, PA, USA, in 1996, and the Ph.D. degree in electrical engineering from Pennsylvania State University, University Park, PA, USA, in 2001.

In 2001, he joined the National Institute of Standards and Technology, Gaithersburg, MD, USA. He is currently a Project Leader with the Wireless Networks Division, Communications Technology Laboratory, Gaithersburg, MD, USA. He has authored over 70 peer-reviewed journal and conference papers and a book on geolocation techniques. His current interests include channel modeling and physical-layer modeling for 5G communication systems.

Peter B. Papazian (SM'98) received the B.S. degree in physics from the State University of New York, Stonybrook, NY, USA, in 1973, and the M.S. degree from the Colorado School of Mines, Golden, CO, USA, in 1979.

He is currently a 5G Millimeter-Wave Channel Sounder Project Leader with the Communications Technology Laboratory, National Institute of Standards and Technology, Boulder, CO, USA. The purpose of this research is to conduct millimeter-wave radio channel propagation measurements to support model and standards development for 5G radio systems.

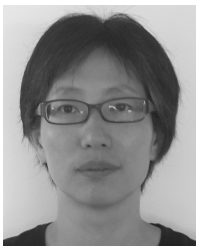

Jian Wang received the B.S. degree in electrical engineering from Tongji University, Shanghai, China, and the M.S. degree in electrical engineering from Washington State University, Pullman, WA, USA.

She was with Nokia, Texas Instruments, and Boeing working on digital signal processing and wireless protocol development. She is currently with the Communication Technology Laboratory, National Institute of Standards and Technology, Gaithersburg, MD, USA. Her current research interests include next generation wireless communications and public safety communications.

Jelena Senic received the B.S. and M.S. degrees in electrical engineering from the School of Electrical Engineering, University of Belgrade, Beograd, Serbia, in 2009 and 2010, respectively.

Since 2015, she has been a Guest Researcher with the National Institute of Standards and Technology, Boulder, CO, USA. Her current research interests include millimeter-wave communications, measurements of signal propagation, and channel modeling for 5G.

Ms. Senic was a recipient of the Best Measurement Paper Award at EuCAP 2017.